ACS APPLIED MATERIALS & INTERFACES

www.acsami.org

Research Article

Plasmonic Gold Trimers and Dimers with Air-Filled Nanogaps

Zachary R. Lawson,[⊥] Arin S. Preston,[⊥] Matiyas T. Korsa,[⊥] Nathaniel L. Dominique, Walker J. Tuff, Eli Sutter, Jon P. Camden, Jost Adam,* Robert A. Hughes, and Svetlana Neretina*

Cite This: *ACS Appl. Mater. Interfaces* 2022, 14, 28186–28198

Read Online

ACCESS | Metrics & More | Article Recommendations | Supporting Information

ABSTRACT: The subwavelength confinement of light energy in the nanogaps formed between adjacent plasmonic nanostructures provides the foundational basis for nanophotonic applications. Within this realm, air-filled nanogaps are of central importance because they present a cavity where application-specific nanoscale objects can reside. When forming such configurations on substrate surfaces, there is an inherent difficulty in that the most technologically relevant nanogap widths require closely spaced nanostructures separated by distances that are inaccessible through standard electron-beam lithography techniques. Herein, we demonstrate an assembly route for the fabrication of aligned plasmonic gold trimers with air-filled vertical nanogaps having widths that are defined with spatial controls that exceed those of lithographic processes. The devised procedure uses a sacrificial oxide layer to define the nanogap, a glancing angle deposition to impose a directionality on trimer formation, and a sacrificial antimony layer whose sublimation regulates the gold assembly process. By further implementing a benchtop nanoimprint lithography process and a glancing angle ion milling procedure as additional controls over the assembly, it is possible to deterministically position trimers in periodic arrays and extend the assembly process to dimer formation. The optical response of the structures, which is characterized using polarization-dependent spectroscopy, surface-enhanced Raman scattering, and refractive index sensitivity measurements, shows properties that are consistent with simulation. This work, hence, forwards the wafer-based processing techniques needed to form air-filled nanogaps and place plasmonic energy at site-specific locations.

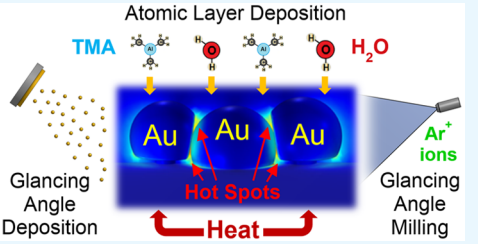

KEYWORDS: *trimer, dimer, nanogap, glancing angle deposition, plasmonic coupling, SERS*

INTRODUCTION

The coupled response obtained when plasmonic nanostructures are placed in close proximity to each other gives rise to a multitude of fascinating properties that, more often than not, eclipse those of standalone nanostructures. Such interactions can lead to (i) electromagnetic fields within the nanogap (i.e., hot spots) that are orders of magnitude greater than those on the perimeter of a standalone structure,[1] (ii) optical phenomena reliant on the hybridization of plasmonic modes,[2,3] (iii) intense interactions with materials confined within the nanogap,[4,5] (iv) plasmon dephasing processes yielding a high density of hot electrons,[6] and (v) for nanogap widths of less than 1 nm, a new set of phenomena collectively referred to as quantum plasmonics.[7] With emerging applications in areas such as (i) the detection of biomarkers for disease,[8,9] explosives,[10] environmentally persistent pollutants,[11] and illicit drugs,[12] (ii) photocatalysis,[13,14] (iii) plasmon-enhanced fluorescence,[15] and (iv) photovoltaics[16] these influences have definitively demonstrated themselves as the foundation for new nanotechnologies. As such, there is a need to advance nanofabrication methods that place parametric controls on plasmonic dimers, trimers, and multimers that allow for tunable light−matter interactions while being responsive to the cost, throughput, and scalability requirements of a nanomanufacturing setting.

Although dimers, trimers, and multimers can be conceptualized as relatively simple constructs, the prevailing situation is one of high complexity resulting from a wide variety of possible nanostructure building blocks, relative orientations, nanogap shapes and widths, and the means by which the integrity of the nanogap is maintained. As a result, the formation of such configurations and their associated structure−property relationships represent a rich and impressive literature spanning colloidal chemistry, directed- and self-assembly, and lithographic techniques.[17−20] Despite these advances, numerous challenges remain. Colloidal techniques, while offering unrivaled capabilities in terms of the accessible building blocks, rely on the use of molecular linkers or dielectric spacers to establish and maintain the nanogap. Occupying the intervening spaces between nanostructures with a secondary material, however, restricts access to the region with the most intense hot spot. Although it is a relatively straightforward task to disperse[21] or form[22−24] colloidal dimers

Received: March 17, 2022
Accepted: May 30, 2022
Published: June 13, 2022

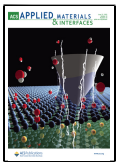

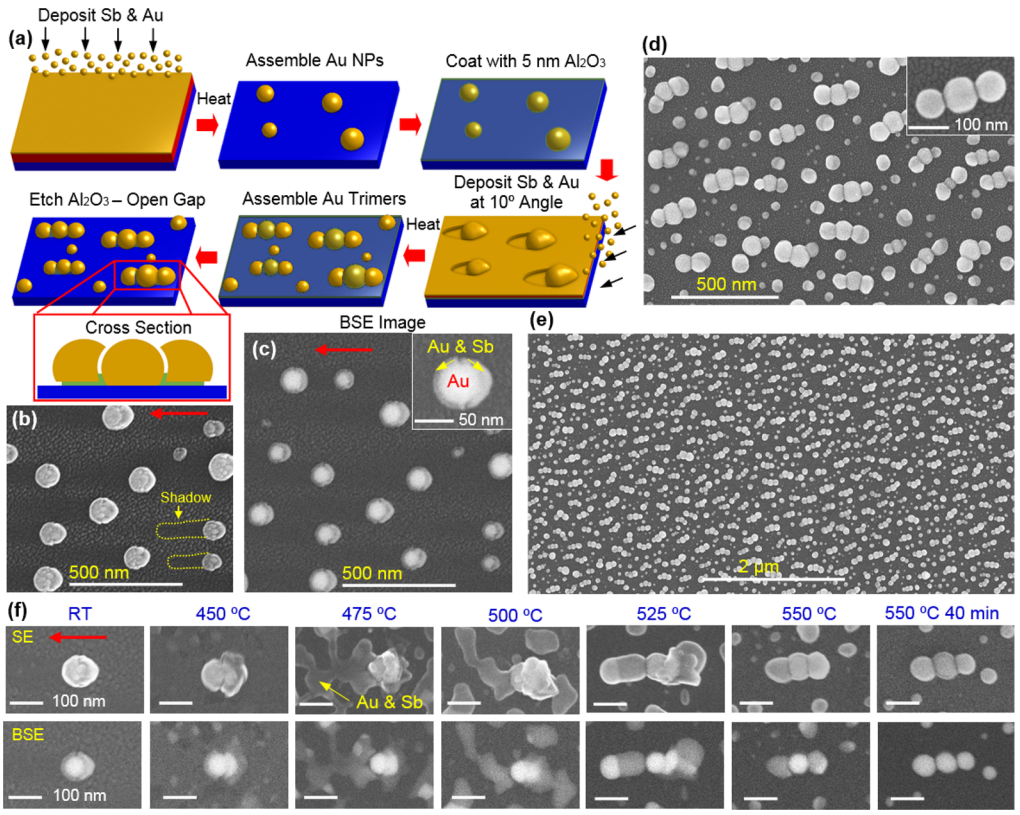

Figure 1. (a) Schematic representation of the procedure used to assemble aligned Au trimers with air-filled vertical nanogaps. (b) SEM image of the sample surface taken after the glancing angle deposition showing egg-shaped structures that have cast a shadow. (c) BSE SEM image of the egg-shaped structures indicating that the central component of the trimer structure has material on its backside after the glancing angle deposition. (d) High- and (e) low-magnification SEM images of the assembled trimers. (f) SE and BSE SEM images showing the assembly of a single trimer that occurs as the temperature is raised from room temperature (RT) to 550 °C. The red arrow in (b), (c), and (f) denotes the direction of the glancing angle deposition.

on substrates, deterministic positioning proves challenging but where progress has been made in this regard using DNA-mediated assembly,[25] laser-scanning-guided assembly,[26] and capillary assembly.[27] In contrast, e-beam lithography (EBL) has demonstrated mastery over nanostructure placement and orientation where air-filled vertical nanogaps allow for analyte entry. Moreover, plasmonic modes that result in hot spots within the vertical nanogap are readily excited by electromagnetic radiation with a wave vector ($\mathbf{k}$) that is perpendicular to the substrate surface. Defining nanostructures separated by nanogaps with widths in the 5 nm range, however, challenges the resolution limits of this technique.[18] With plasmonic hot spot intensities critically dependent on the nanogap width,[28] this limitation is onerous and compounded by the low-throughput, technically demanding, and cost-prohibitive nature of the EBL technique. Given this situation, there is the incentive to advance low-cost techniques for forming nanogaps that mitigate these deficiencies while still using the toolset associated with wafer-based processing.

Atomic layer deposition (ALD)[29] has emerged as a mainstream wafer-scale processing technique for the deposition of ultrathin oxide layers. It is unique in its ability to deposit conformal films on irregularly shaped surfaces where the layer thickness can be controlled with monolayer-scale precision. As such, it has increasingly been integrated into leading-edge nanofabrication schemes directed toward the generation of functional plasmonic nanomaterials. Examples include the use of ALD-deposited oxides as (i) spacer materials between opposing metal nanostructures,[28,30−32] (ii) claddings for vulnerable metals (e.g., Ag, Cu) against oxidation and harsh chemical environments,[33,34] (iii) protective shells able to maintain nanostructure shape and faceting at high temperatures,[33,35,36] (iv) agents able to direct nanometal syntheses,[37] (v) dielectrics between nanogap electrodes,[38] (vi) metamaterial components offering subwavelength optical confinement,[39−43] and (vii) dielectric spacers for applications in shell-isolated nanoparticle-enhanced Raman spectroscopy (SHINERS)[44] and shell-isolated nanoparticle-enhanced fluorescence (SHINEF).[15] Taken together, this work highlights the strengths of the ALD technique. Specifically, it demonstrates the effectiveness of ALD in forming conformal oxide layers on the subnanometer length scales that are inaccessible to the EBL technique, a capability that has been exploited to fabricate precisely defined dielectric-filled nanogaps for metamaterials,[39−43] nanoparticle on mirror (NPoM) configurations,[45] and various nanostructure assemblies.[30−32] Other nanofabrication schemes have selectively removed the dielectric to form air-filled nanogaps[30,46,47] by capitalizing on the susceptibility of ALD-deposited amorphous Al_2O_3 to relatively mild wet etchants.[33,47]

With physical vapor deposition (PVD) techniques being integral to wafer-based processing, there has also been an impetus to incorporate innovative PVD-based schemes into nanofabrication. Among these, the glancing angle deposition (GLAD)[48] technique has emerged as a processing tool of significance due to an ability to induce asymmetries into

https://doi.org/10.1021/acsami.2c04800
ACS Appl. Mater. Interfaces 2022, 14, 28186−28198

material depositions caused by the incident flux of atoms being subject to the shadowing influences of substrate-based surface features. Such schemes have, for example, been used to (i) form chiral structures,[49] (ii) deterministically deposit material within holes formed in patterned resists or self-assembled colloids,[50−52] and (iii) assemble dimer arrays separated by dielectric-filled vertical nanogaps.[32] The dimer demonstration uses block copolymer micelle nanolithography to form an array of Au nanostructures that is then coated with an ultrathin oxide and subjected to a glancing angle deposition where a substrate manipulator places precise controls over both its tilt and azimuthal angles relative to the incident flux of Au atoms. The technique, while impressive, has drawbacks in that it uses specialized deposition equipment, demands that the array be exceedingly dense so that the bare substrate areas between structures are shadowed, and requires that the initial array have long-range order for the azimuthal angle adjustment to prove meaningful. Also noteworthy is that glancing angle ion milling, which represents the subtractive analogue to the GLAD technique, has also been used in the processing of plasmonic materials.[42]

In prior studies, we have shown that the solid-state dewetting of a Au film at high temperatures can be radically altered by a sacrificial Sb underlayer that sublimates as the Au assembles into nanostructures.[53,54] The inclusion of Sb into the assembly process dramatically increases the characteristic length scale over which Au accumulates to form individual nanostructures. With the Au and Sb layer thicknesses acting as adjustable parameters, the combination allows for the independent variation of the size and spacing of assembled nanostructures, a capability that is unattainable when using the conventional solid-state dewetting[55] technique. Herein, we demonstrate a substrate-based nanofabrication process for the formation of aligned trimers composed of Au nanostructures separated by air-filled vertical nanogaps. The process, which utilizes PVD, ALD, GLAD, high-temperature self-assembly, and wet-etching processes, capitalizes on the remarkable properties of a sacrificial Sb layer in directing Au assembly. The approach is also extended to the fabrication of arrays of aligned trimers and dimers by imposing a periodicity onto the assembly process using a benchtop nanoimprint lithography technique. The work, hence, advances the use of wafer-based processing tools as a means to fabricate plasmonic nanogaps without the need for the demanding lithographic steps associated with EBL.

RESULTS

Nanofabrication of Au Trimers with Air-Filled Nanogaps. Figure 1a shows a schematic of the devised nanofabrication process for the assembly of substrate-based gold trimers with air-filled vertical nanogaps. The stepwise procedure begins with the sequential deposition of Sb and Au films on a single-crystal Al_2O_3 substrate (i.e., sapphire). This is followed by a high-temperature assembly process carried out in a quartz tube furnace under an Ar gas flow that gives rise to standalone Au nanostructures. A conformal layer of amorphous Al_2O_3 is then deposited over the entire surface using ALD. The so-formed Au structures ultimately act as the central component of the trimer structure where the oxide thickness defines the nanogap width. Trimer formation proceeds through the sequential deposition of Sb and Au at a glancing angle followed by a second high-temperature assembly process carried out in a similar manner. Accompanying trimer assembly is the formation of a population of standalone Au nanoparticles with diameters that are consistently smaller than those that make up the trimer. A wet chemical etch is then used to remove the amorphous oxide, leaving Au trimers with air-filled nanogaps. The overall procedure, while highly reproducible, leads to a counterintuitive result in that one of the three trimer components forms at the precise location where it is least expected, i.e., the backside region that is shadowed in the glancing angle deposition. An understanding of this peculiar finding, as well as the requirements for optimal trimer assembly, requires the step-by-step analysis of the entire process that is presented below.

The initial formation of standalone Au nanostructures and their encapsulation in an ultrathin Al_2O_3 coating are well-described by prior work.[33,53] From the standpoint of the trimer fabrication, the use of a sacrificial Sb layer allows for the size and spacing of the central particle to be tailored such that the resulting interparticle distance provides sufficient room for the trimers to form while, at the same time, being dense enough to provide a high level of shadowing to the substrate surface during the subsequent glancing angle deposition. The optimization of the Sb layer thickness (Figure S1) led to an average Au nanostructure diameter, interparticle spacing, and areal density of 55 nm, 180 nm, and 5×10^8 cm^{-2}, respectively. The resulting Au structures (i) display a single-crystal character with their [111]-orientation normal to the substrate surface,[56] (ii) have a truncated sphere morphology due to the flat interface formed with the substrate, and (iii) exhibit a prominent localized surface plasmon resonance (LSPR) near 560 nm that red-shifts to 570 nm when a 5 nm thick amorphous Al_2O_3 coating is applied (Figure S2). The use of an ALD-deposited Al_2O_3 layer is crucial to trimer formation in that it (i) provides a conformal spacer material that can be deposited with nanometric precision, (ii) can withstand high temperatures, and (iii) has favorable wet-etching characteristics. With the Au nanostructures well-bonded to the substrate and the oxide encapsulation layer negating Au surface diffusion pathways, these structures remain stationary and morphologically stable throughout the trimer assembly process.

The glancing angle deposition is carried out at a 10° angle with respect to the surface of the substrate to promote the preferential deposition of Sb and Au onto one side of the Al_2O_3-coated Au structures (Figure S3a). SEM images taken immediately after the sputter deposition show coated structures with an egg-shaped appearance where each has generated a sizable shadow (Figure 1b and Figure S3b). A substantial percentage of the exposed substrate surface, however, remains unshadowed. SEM backscattered electron (BSE) images taken after the deposition (Figure 1c) reveals that the material deposited onto the Al_2O_3-coated Au nanostructures does not take on the morphology expected for a hit-and-stick glancing angle deposition. Instead, it shows a morphology that requires adatom diffusion to the backside of the structure. Diffusion is enabled by the fact that atoms arrive to the surface with significant kinetic energy derived from the Ar^+ ion accelerating voltage of 6 keV used in the sputtering process. It should be noted that significant Au diffusion over the length scales of relevance has been observed for depositions carried out at room temperature.[57] The imperfect directionality associated with the sputter deposition is also a contributing factor. Energy dispersive X-ray spectroscopy (EDS) elemental analysis reveals that Sb and Au diffusion is

https://doi.org/10.1021/acsami.2c04800
ACS Appl. Mater. Interfaces 2022, 14, 28186−28198

also occurring into the shadowed regions directly behind the Al_2O_3-coated Au nanostructures (Figure S4a). These results therefore indicate that the glancing angle deposition does not result in ideal shadowing but instead leads to a gradient of material on and around each of the initially formed structures. After this deposition, all areas of the substrate have been coated to some degree, with even the heavily shadowed regions experiencing some level of Au−Sb deposition.

The assembly of trimers from the GLAD-deposited material proceeds as the sample is heated to 550 °C and then held there for 40 min before a slow cool to room temperature. This heating regimen is crucial to the success of the overall process since its upper temperature has to be sufficiently high to cause Sb sublimation and Au agglomeration but not so high as to initiate the crystallization of the amorphous Al_2O_3 layer. The latter is of the utmost importance to the formation of air-filled nanogaps since the crystalline phase of Al_2O_3 is not readily etched. The onset of crystallization at somewhat higher temperatures (i.e., 600 °C), which was determined empirically through etching experiments, is consistent with the findings of Broas et al.[58] Figure 1d,e shows SEM images of the assembled trimers interspersed with smaller standalone nanoparticles and the occasional dimer. Striking is the degree of trimer alignment achieved for an assembly process that is lithography-free. The unwanted standalone particles form in areas where Sb and Au landed directly on the substrate. Minimizing their numbers below what is shown in the images is possible by increasing the density of the Al_2O_3-encapsulated Au structures, but this is done at the expense of having many trimers intersect with one another (Figure S5). The importance of the sacrificial Sb layer in this assembly process is made evident by the complete absence of trimer structures when the glancing angle deposition is performed without it (Figure S6). Instead of forming trimers, the Al_2O_3-encapsulated Au structures become freckled with as many as 10 nanoparticles with the intervening spaces populated with a dense distribution of small Au nanoparticles. Similarly, the importance of the glancing angle deposition is made evident by the unsatisfactory assembly process obtained when Sb and Au are deposited at an angle of incidence that is normal to the substrate surface (Figure S7). It should be noted that EDS elemental analysis shows that any residual Sb within the trimer structures is below levels that are detectable (Figure S4b).

To gain additional insights into the trimer assembly, a series of samples were produced in which the assembly process was initiated by heating the sample in the usual manner but then halted at various stages through a rapid quench brought about by opening the furnace lid and then blowing room temperature air onto the quartz tube housing the sample. Obtained is the progression displayed in Figure 1f showing representative secondary electron (SE) and BSE SEM images that show the deposited material assembling into a trimer structure as Sb is gradually lost to the vapor phase. When examining this progression, it is cautioned that such a portrayal can, at times, be deceptive due to the existence of a Au−Sb eutectic that will render Sb-rich combinations as a miscible liquid at the high temperatures shown. Moreover, there is a tendency for the liquid to phase-separate upon cooling for those Au−Sb combinations that are immiscible in the solid state. Notwithstanding, there are clear indications that the thicker unshadowed regions assemble first to form either the front component of the trimer or standalone nanostructures. This leaves an isolated tail at the back side of the forming trimer that then, upon further heating, assembles into its back component.

On the basis of these findings, it is evident that Sb plays a pivotal role in the assembly of both standalone Au nanostructures and trimers. From a mechanistic standpoint, Sb has two important properties in that it (i) forms a low-temperature eutectic with Au ($T_E \approx 360$ °C) and (ii) readily sublimates at temperatures of relevance to the assembly process. In the assembly of standalone Au nanostructures, which is shown schematically in Figure 2a, a Au−Sb bilayer is

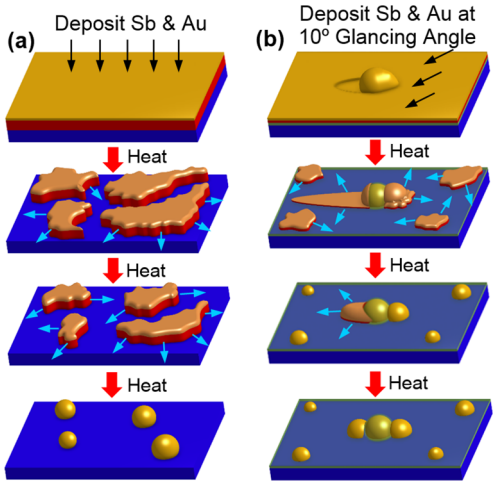

Figure 2. Schematics illustrating the mechanisms by which (a) standalone Au nanostructures and (b) Au trimers are assembled using a sacrificial Sb layer. The blue arrows denote Sb sublimation from the sides of the pedestals.

deposited and then heated to temperatures that see the breakup of the layers, Sb sublimation, and the formation of a thin AuSb liquid layer atop the remaining Sb pedestals. It is this transformation from the solid to liquid state that allows for the assembly of Au over much larger length-scales than those possible in the solid-state dewetting of a Au film performed in the absence of Sb. Another important feature of the assembly process is that the AuSb liquid layer inhibits Sb sublimation from the top surface, creating a situation where the underlying Sb layer is able to sublimate from its edges at a much greater rate. This creates a situation where the underlying Sb pedestal is shrinking from all sides, forcing the AuSb liquid toward its center. With continued heating, all of the Sb is lost to the vapor phase, leaving Au nanostructures resting on the surface of the substrate. Studies supporting this mechanism have been reported previously.[53,54] Trimer formation, which is shown schematically in Figure 2b, utilizes many of the same properties of the Au−Sb system. In this case, however, there exists a gradient of Au and Sb due to the shadowing effects associated with the glancing angle depositions. In this scenario, the thicker unshadowed regions tend to break up earlier in the assembly process, leaving the shadowed layers more or less intact so as to form a tail at the back side of each of the forming trimers. As the temperature is increased further, the tail region forms a AuSb liquid on its surface but where, in this case, Sb sublimation is only possible from three of its sides since access to the fourth side is blocked by the central component of the trimer. With access blocked, the Au−Sb liquid is forced to the back side of the trimer instead of toward the center of the pedestal. Continued heating results in the

https://doi.org/10.1021/acsami.2c04800
ACS Appl. Mater. Interfaces 2022, 14, 28186−28198

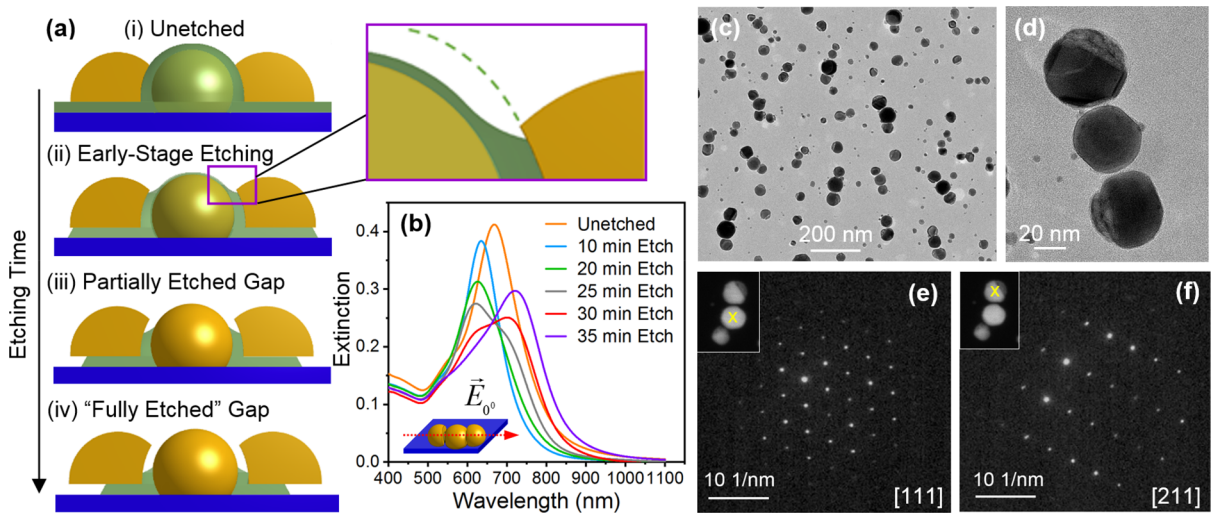

Figure 3. (a) Schematic representation showing the time evolution of the etching process that removes the amorphous Al_2O_3 layer from the nanogap and partially undercuts the front and back components of the trimer structure. (b) Extinction spectra showing the time evolution of the LSPR as the amorphous Al_2O_3 is progressively etched. (c, d) Low- and high-magnification TEM images of fully etched Au trimers assembled on a Si_3N_4 TEM window grid. Nanobeam electron diffraction (NBD) patterns for the (e) central and (f) back trimer nanoparticles.

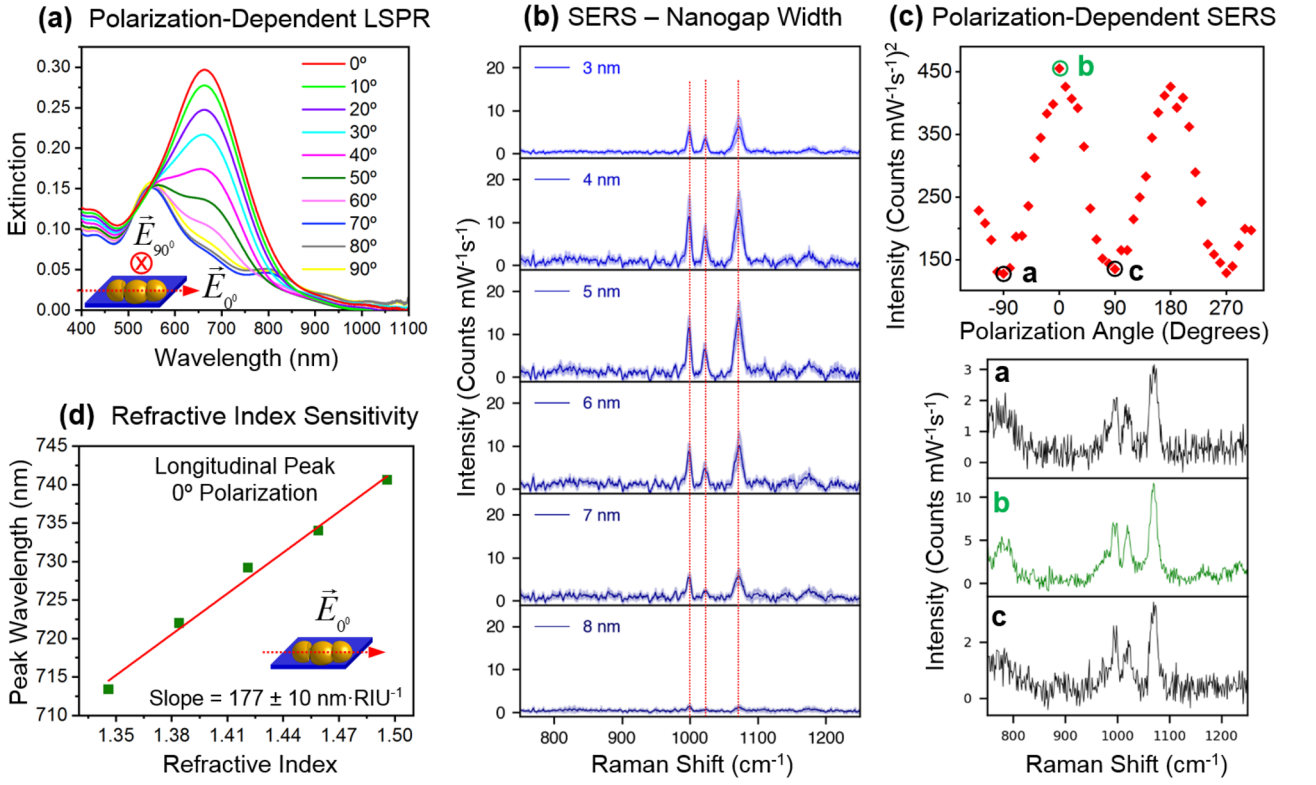

Figure 4. (a) Polarization-dependent extinction spectra for Au trimers where the dielectric within the nanogaps has been optimally etched. The inset shows the trimer orientation relative to the polarization direction. (b) SERS spectra for benzenethiol detection by Au trimers where the nanogap width is varied between 3 and 8 nm. (c) Polarization-dependence of the integrated benzenethiol SERS intensity for the spectral region between 980 and 1080 cm^{-1} where 0° and 90° angles correspond to light that is polarized parallel and perpendicular to the long axis of the trimer, respectively. Below the polarization dependence are three representative spectra corresponding to the points denoted by a, b, and c. (d) Refractive index sensitivity measurements for the longitudinal mode.

complete loss of Sb, leaving a Au trimer separated by Al_2O_3-filled nanogaps.

The removal of the Al_2O_3 dielectric from the nanogaps is achieved using aqueous NaOH (5 mL, 10 mM). This etchant is selective in that it dissolves amorphous Al_2O_3 while leaving both the Au nanostructures and crystalline Al_2O_3 substrate intact. It should, however, be recognized that excessive etching is problematic since both the front and back trimer nanoparticles are resting on the amorphous layer and, as such, can become disconnected from the substrate surface through undercutting. Figure 3a shows a schematic illustrating the time dependence of the etching process where it is

https://doi.org/10.1021/acsami.2c04800
ACS Appl. Mater. Interfaces 2022, 14, 28186−28198

assumed that the etching of amorphous Al_2O_3 is spatially uniform and controllable, an assumption supported by prior work.[33] At the onset of the etching process neither the dielectric within the nanogap nor that beneath the front and back components of the trimer structure is exposed to the etchant since they are shielded by the adjacent Au and amorphous Al_2O_3. This situation, however, gradually changes as the exposed layer thins. It is, hence, anticipated that most of the initially exposed layer is removed before significant nanogap etching or undercutting occurs. At this stage, the exposed dielectric within the nanogap is continuously removed where etch fronts exist on both the top and side surfaces. The undercutting of the front and back structures occurs in a similar manner. Because the etching process must be terminated before complete undercutting occurs, the final trimer structure takes on an unusual morphology in which air-filled nanogaps exist but where some of the dielectric remains.

With the etching process proving critical, it became advantageous to spectroscopically monitor it over time where spectral signatures were identified that indicate the formation of air-filled nanogaps as well as trimer destruction when excessive undercutting occurs. Such signatures allow for an appropriate termination to the etching process. Figure 3b shows representative extinction spectra for light polarized parallel to the long axis of a trimer with a nanogap width of 5 nm. As the etching process begins, the LSPR peak blue-shifts and weakens and then red-shifts and strengthens. An analysis of this behavior, based on both experiment and simulation (vide infra), indicates that the blue shift is the desired response needed to obtain nanogaps whereas the red shift demarcates an overetching that is destructive to the trimer structure. Similar etching experiments performed on trimers with nanogaps ranging from 3 to 8 nm show a similar response where in all cases the optimum etching time is approximately 25 min (Figure S8). Figure 3c,d shows low- and high-magnification TEM images for etched Au trimers assembled directly on a Si_3N_4 TEM grid. Although the assembly of trimers on grids is less than optimal, the images still show trimer structures with well-defined nanogaps. Nanobeam electron diffraction (NBD) patterns (Figure 3e,f) show that the trimer components have a crystalline character with the central and back particles shown having their [111]- and [211]-axis normal to the Si_3N_4 surface, respectively.

Optical Characterization and Simulations. The trimers produced in this self-assembly process are distinct in that (i) they exhibit a high degree of alignment, (ii) all three components have nonspherical geometries, (iii) their bottom surfaces have some areas that are resting on Al_2O_3 while others are suspended, and (iv) they exhibit nanogaps that are defined by curved sidewalls and that are occupied by a mixture of air- and Al_2O_3-filled regions. Given that a plasmonic response is highly sensitive to nanostructure shape, coupling phenomena with nearby structures, and the adjacent dielectric environment, it is not surprising that these distinctive properties express themselves in the optical properties of trimers. Figure 4a shows the polarization-dependent extinction spectra for an optimally etched trimer sample. The sample was illuminated with linearly polarized light where the 0° polarization aligns with the long axis of the trimer. It exhibits a strong polarization dependence where the anticipated longitudinal and transverse LSPR features are clearly visible for the 0° and 90° polarizations, respectively. A weak resonance also appears near 800 nm whose origin is unclear but may be associated with a Fano resonance.[59]

The etched trimers allow for the placement of analytes within the nanogap and are, hence, of interest to both SERS and refractive index sensing. SERS measurements were carried out on six samples where the nanogap width was varied between 3 and 8 nm in 1 nm increments. Benzenethiol, which is a relatively weak Raman scatterer known for its ability to form a self-assembled monolayer on Au surfaces,[60] was used as the reporter molecule. Figure 4b shows the SERS data for the spectral range where benzenethiol is known to exhibit peaks at 999, 1022, and 1074 cm^{-1}. Each spectrum represents an average of seven measurements where the shaded area provides 95% confidence intervals. The overall trend sees the expected increase in Raman intensity as the nanogap width is reduced except for a reversal in the trend for the smallest width. The unexpected loss in intensity for low widths could indicate that the 3 nm Al_2O_3 spacer used in trimer formation lacks the robustness needed to endure the high-temperature assembly process or that the etching process for the narrowest nanogaps requires optimization. Polarization-dependent measurements performed on trimers with a 5 nm nanogap (Figure 4c) show that integrated benzenethiol SERS intensity for the spectral region between 980 and 1080 cm^{-1} exhibits a sinusoidal pattern where the maximum intensity occurs for light polarized along the long axis of the trimer. The result provides evidence that the SERS signal originates from benzenethiol molecules within the nanogap. This conclusion is corroborated by measurements that compare the SERS spectra before and after the Al_2O_3 dielectric within the nanogap is etched away in that they show that dielectric-filled nanogaps are unable to detect benzenethiol (Figure S9). Figure 4d shows the refractive index sensitivity data for the longitudinal mode obtained by immersing the sample in various mixtures of acetonitrile and toluene. The data yield a refractive index sensitivity of 177 nm·RIU^{-1} for the longitudinal mode, whereas the transverse mode shows an insensitivity to changes in the refractive index (Figure S10). Also noteworthy is that refractive index sensitivity degrades for longer etching times, a further indication that excessive etching leads to trimer degradation.

With the nanogap width and the degree of Al_2O_3 etching providing readily varied experimental parameters that significantly alter the plasmonic response of trimers, simulations were carried out that place emphasis on determining their role and significance. The methods used and calculation details are described in the Supporting Information. The geometric model used to predict trimer properties (Figure S11) mimicked the experimentally observed structure. The model assumes that the nanogaps are uniformly etched from all exposed sides and that the front and back components of the trimer structure are simultaneously undercut at the same rate. The blue shift caused by the initial removal of amorphous Al_2O_3 from the exposed surfaces of the central component of the trimer structure (i.e., Figure 3a, step ii) is not modeled so that emphasis can be placed on describing the influence that etching material from the nanogap has on the optical properties (i.e., Figure 3a, steps iii and iv). For all cases, the optical response was calculated for light having an incident wave vector ($\mathbf{k}$) normal to the substrate surface where its electric field ($\mathbf{E}$) was polarized to excite either transverse or longitudinal plasmon modes.

Figure 5a shows the simulated extinction spectra for the longitudinal plasmon modes for three trimer structures having

https://doi.org/10.1021/acsami.2c04800
ACS Appl. Mater. Interfaces 2022, 14, 28186−28198

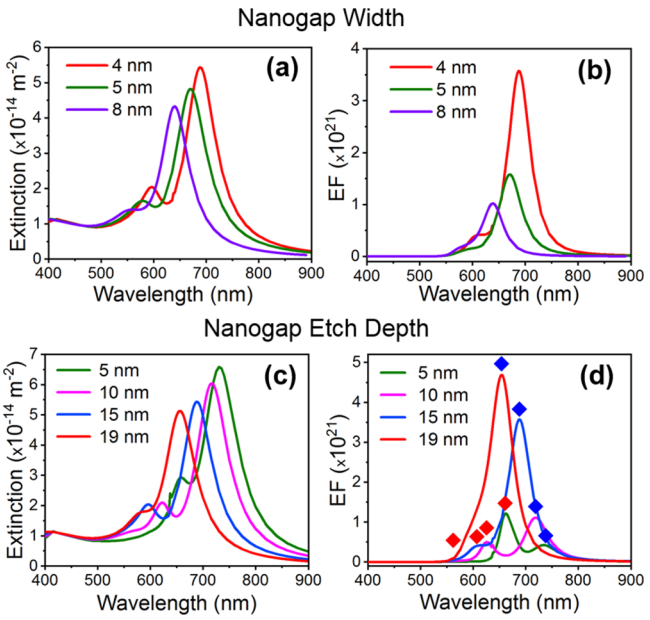

Figure 5. Spectral dependence of the (a) extinction cross section and (b) near-field enhancement factor for the longitudinal mode of trimers with a nanogap etch depth of 15 nm and widths of 4, 5, and 8 nm. Spectral dependence of the (c) extinction cross section and (d) near-field enhancement factor for the longitudinal mode of trimers with a nanogap width of 4 nm and etch depths of 5, 10, 15, and 19 nm.

nanogap widths of 4, 5, and 8 nm. For all three cases, the spectra represent etched structures where 15 nm of amorphous Al_2O_3 has been removed from all exposed sides of the nanogap and where an equally sized undercut is placed under the front and back components of the trimer. Each of the spectra show a prominent LSPR peak that red-shifts and increases in magnitude as the nanogap width decreases as well as a weaker mode at lower wavelengths that behaves similarly. The trends observed are in agreement with the measured spectra (Figure S12). The transverse mode is weaker and remains largely unchanged over the same range of nanogap widths (Figure S13a). Such tendencies are in line with those experimentally observed and simulated for dimer structures.[61−63]

Figure 5b shows the spectral dependence of the surface averaged near-field enhancement factor (EF) for the same three trimer configurations where near-fields that exist within the dielectric are excluded from the calculations. This exclusion allows for a more accurate prediction of the near-fields accessible in SERS because only air-filled regions allow analyte entry. The 4 nm nanogap shows the largest enhancement over most of the spectral range where the maximum value occurs at its resonant frequency. The result is as anticipated since narrow nanogaps lead to stronger electromagnetic field confinement. The enhancement factor for the transverse mode is, once again, weaker and similarly sized for all three cases (Figure S13b). Near-fields for the three nanogap widths were calculated for both the longitudinal and transverse modes (Figures S14 and S15). The width dependence follows anticipated behaviors in that the (i) near-fields of the longitudinal mode within the nanogaps markedly increase in strength as its width is reduced, (ii) maximum near-fields of the transverse mode are significantly weaker than those of the longitudinal mode, and (iii) near-field intensities peak at the resonant frequency.

Figure 5c shows the simulated extinction spectra for trimers with a nanogap width of 4 nm that are "etched" from all sides to depths of 5, 10, 15, and 19 nm. The 19 nm value was chosen to represent a fully etched trimer since somewhat larger values would completely undercut the smaller side particle, leaving it hovering above the substrate surface. Each of the calculated spectra show a dominant mode that blue-shifts as more of the dielectric within the nanogap is removed as well as a weaker mode that behaves similarly. This behavior is consistent with the experimentally observed blue shift that is evident in Figure 3b for etch times that are less than 25 min. The experimentally observed red shift that is accompanied by an increase in extinction for etch times greater than 25 min could not be simulated for any level of etching including the unphysical

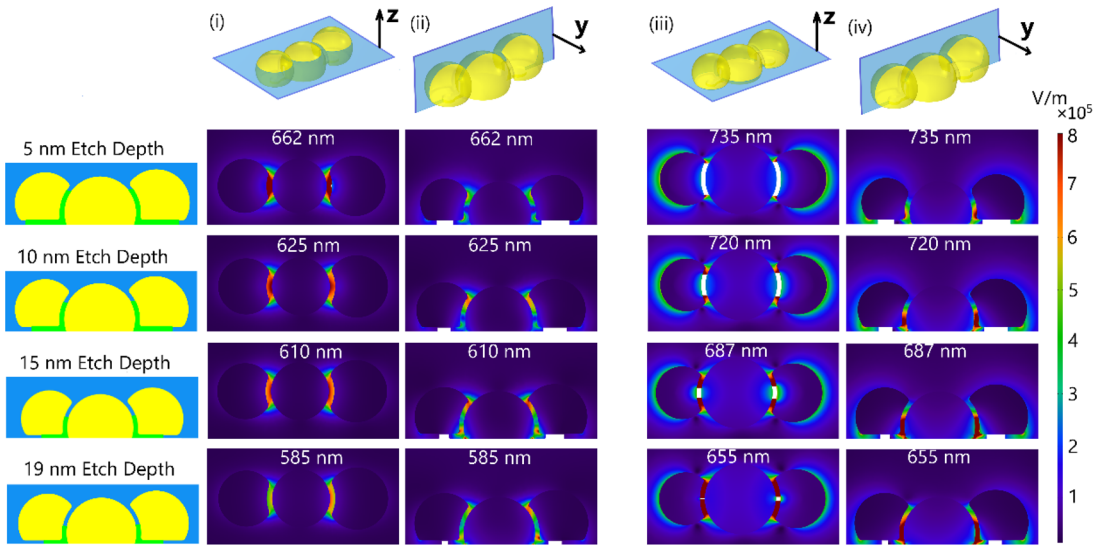

Figure 6. Color maps showing the near-fields at the resonant wavelength for the Au trimer plasmon modes with a 4 nm nanogap width and nanogap etch depths of 5, 10, 15, and 19 nm. The schematic above each column indicates the cross section used for the map, while the schematic adjacent to each row shows the etched configuration. Each color map is labeled with the wavelength of the incident light that is polarized along the long axis of the trimer. Areas where the cross section intersects the amorphous Al_2O_3 layer are shaded in white.

https://doi.org/10.1021/acsami.2c04800
ACS Appl. Mater. Interfaces 2022, 14, 28186−28198

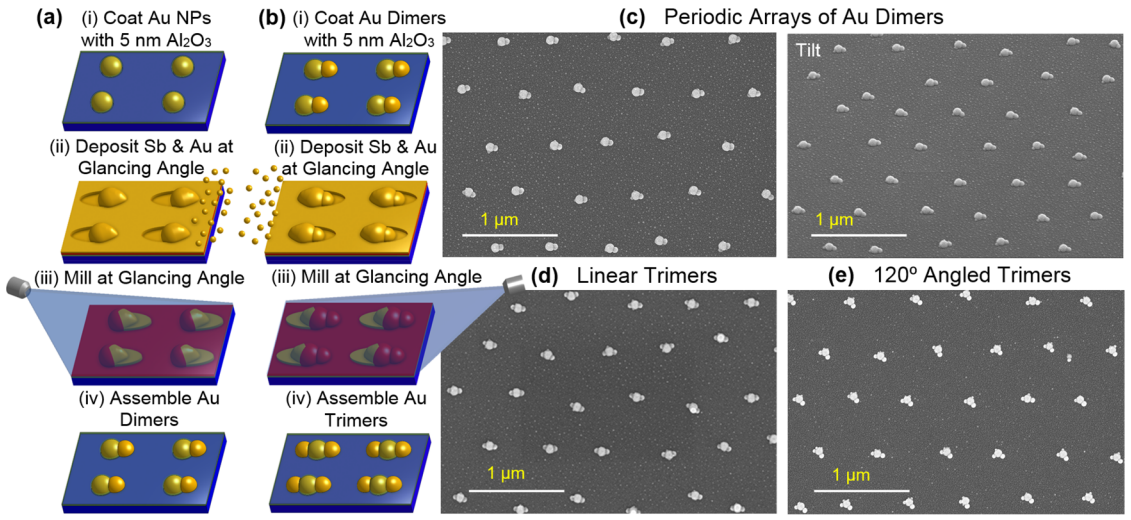

Figure 7. Schematic representation of the procedure used to fabricate periodic arrays of Au (a) dimers and (b) trimers. SEM images of an array of (c) dimers, (d) linear trimers, and (e) 120° angled trimers.

scenario where the entire dielectric is removed and the front and back components of the trimer structures are levitating above the substrate surface. The experimentally observed red shift is, however, expected if the front and back structures were being pulled toward the central component of the trimer structure so as to reduce or even collapse the nanogap. Such a collapse would not be surprising given that the capillary forces arising when drying the liquid etching solution from the nanogap would tend to pull the structures together. These simulations, hence, lend credence to the assertion that the observed red shift is associated with trimer degradation.

Figure 5d shows the simulated EF spectrum for the same four etch depths where the contributions from the dielectric-filled regions are, once again, excluded. Immediately evident is that the overall trend when comparing the four different nanogap etch depths is opposite to that shown in the extinction spectra (Figure 5c). This is a direct result of the exclusion of near-fields within the dielectric when calculating the EF value. The largest EF occurs for the deepest etch depth (i.e., 19 nm). A closer inspection reveals that there are two peaks associated with each of these curves where one, denoted by the blue diamonds, blue-shifts and increases in strength as the etch depth is increased while the other, denoted by the red diamonds, blue-shifts and decreases in strength. Insights into this behavior are more readily obtained through an examination of the spatial distribution of the near-fields resulting from each of these etch depths.

The dielectric environment around the Au trimer is unique in that it is characterized by a complex arrangement of air−Au, Al_2O_3−Au, and air−Al_2O_3 interfaces where the exact configuration is determined by the degree of etching carried out. As such, the distribution of near-fields is also complex and variable. Simulations reveal that, as expected, the most intense near-fields reside within the nanogap. It should, however, be appreciated that the etching of the dielectric within both the front and back nanogaps proceeds from all exposed sides to form an air-filled region taking on a ∩-shape that is slightly bent to conform with the curved sidewalls of the nanogap. With continued etching, the ∩-shaped regions grow in width as the dielectric is reduced to an L-shaped nub with one of its arms in the nanogap while the other extends under the front or back component of the trimer. Figure 6 shows color maps of the simulated near-fields for trimer cross sections and etch depths shown in the adjacent schematics where the incident light is polarized along the long-axis of the trimer. Areas where the cross section intersect the dielectric are shaded in white. It should be noted that the position of the cross section, as denoted by the z- and *y*-axes, was varied somewhat depending on the etch depth so as to reveal the hot spot of most relevance. The analysis reveals that the air-filled space within the nanogap displays two distinct regions where intense near-fields form. The first, which is made apparent by the two cross sections labeled (i) and (ii), shows that a hot spot exists near the upper extent of the dielectric that weakens and blue-shifts as the etch depth is increased. It is this hot spot that gives rise to the peaks in the EF spectra denoted by the red diamonds in Figure 5d. The second, which is made apparent by the two cross sections labeled (iii) and (iv), shows the presence of a hot spot that runs down the sides of the dielectric within the nanogap that blue-shifts and grows in intensity as the etch depth is increased. It is this hot spot that gives rise to the peaks in the EF spectra denoted by the blue diamonds in Figure 5d. Four representative videos that provide a more complete view of the near-fields surrounding a trimer with a 15 nm etch depth (i.e., the third row) by scanning through cross sections along its width and depth are supplied as Supporting Information.

Forming Periodic Arrays of Dimers and Trimers. Numerous examples exist where lithographically defined features are used to regulate self-assembly processes to create ordered arrangements of nanostructures.[64,65] Such pathways also provide the opportunity for the deterministic positioning of plasmonic nanogaps and, in doing so, allow for the confinement of light energy at site-specific locations. Previously, we have demonstrated a benchtop nanoimprint lithography (NIL) process for generating large-area periodic arrays of Au nanostructures.[66,67] By applying these same techniques, it is a relatively straightforward process to generate periodic arrays of trimers. There is, however, a significant problem in that arrayed structures shadow only a small percentage of the exposed substrate surface during the glancing angle deposition since they have a rather large periodicity of 600 nm. As a result, trimer assembly is accompanied by the formation of a dense background of Au nanostructures whose numbers far exceed those of trimers (Figure S16). To resolve

https://doi.org/10.1021/acsami.2c04800
ACS Appl. Mater. Interfaces 2022, 14, 28186−28198

this issue, a scheme was devised to rid the surface of this dense background while allowing for the formation of both dimers and trimers.

Periodic arrays of Au nanostructures were formed using the aforementioned NIL technique and then, using ALD, coated with a 5 nm thick layer of amorphous Al_2O_3. These oxide-coated nanostructures are then subjected to the process shown schematically in Figure 7a. The structure is first exposed to sequential glancing angle depositions of Sb and Au that preferentially deposit material onto one side of the structure while still having a substantial amount of material land directly on the substrate surface. A thin layer of material is then removed from the surface using an oppositely directed glancing angle ion milling procedure. Milling conditions are optimized to remove Au from the surface that would otherwise form a dense background while leaving most of the underlying Sb intact. Material is also removed from one side of the arrayed structure while the other side is protected due to the effect of self-shadowing. When heated, the structure assembles into a dimer because the milling procedure also removes the Au that would otherwise form the third trimer particle. The oxide within the nanogap can then be etched away in the usual manner. Figure 7c shows an SEM image of the dimer array produced where the dense background has largely been eliminated. The image shows a high degree of dimer alignment where it is evident that the assembled structure is somewhat smaller than expected based on the results shown in Figure 1d. This reduction in size is also associated with a loss of Au to the ion milling process.

The procedure by which periodic arrays of dimers are produced can be extended to the fabrication of trimers using the process schematically shown in Figure 7b. It begins by producing a periodic array of Au dimers but where no Al_2O_3 etching procedures are performed. It then applies the same glancing angle deposition procedure used to form dimers apart from the fact that the sample is rotated in-plane by 180° so that material preferentially deposits on the exposed side of the oxide-coated nanostructure. An oppositely directed glancing angle milling procedure is then applied to remove unwanted Au, after which the sample is heated to form trimers. Figure 7d shows an SEM image of an array of aligned trimers where it should be noted that the oxide-free dimer structure that faced the milling direction appears unscathed. This is likely due to the fact that it was protected by a thin layer of Sb similar to that shown in the inset to Figure 1c. The trimer formation process also allows for some degree of control over the trimer configuration by applying the glancing angle deposition at an in-plane angle of 120° (as opposed to 180°) followed by an oppositely directed glancing angle ion milling procedure. Such a scenario results in nonlinear trimers that express the in-plane angle used in the glancing angle deposition (Figure 7e). These capabilities overlap with those demonstrated by Jeong et al.[32] but where the use of Sb in combination with glancing angle ion milling allows for the formation of arrays with near-arbitrary pitch.

DISCUSSION

The self-assembly route described herein is unique in its ability to fabricate aligned Au trimers with vertical air-filled nanogaps without the need for lithographic steps. Its success is reliant on the use of Sb and amorphous Al_2O_3 as sacrificial materials as well as the GLAD technique. Sb is crucial for its ability to enhance the areal extent over which Au collects when forming the front and back components of the trimer structures. Amorphous Al_2O_3 provides the means to define a nanogap width with a precision that eludes conventional EBL techniques. GLAD imparts a directionality to the assembly process that leads to trimer formation and alignment. Together they unite to form photonic surfaces with plasmonic hot spots and a polarization-dependent response. Despite this achievement, the assembly process has its downsides in that (i) the degree of trimer alignment achieved is far from perfect, (ii) it yields a substantial trimer size distribution as well as a sizable population of standalone nanostructures, and (iii) the three trimer components have rounded morphologies that are suboptimal when trying to maximize near-field intensities.

Many of the deficiencies observed for trimer self-assembly are, however, lessened when the lithographically defined features accessible through NIL are used to regulate the assembly process. This transformation from a self-assembly to a directed-assembly process not only gives rise to periodic arrays but also is accompanied by an increase in size uniformity that results from the fact that the central component of the trimer is produced with a near-identical size and shape. With the shadow cast by each structure being identical in the glancing angle deposition and the unwanted shadowing of adjacent particles being eliminated due to a well-defined periodicity, the assembly process occurring at each of the arrayed sites becomes more uniform and results in a higher degree of alignment. The organized nature of the array also allows for a glancing angle ion milling procedure that is able to rid the surface of unwanted standalone nanostructures and allows for the formation of both dimers and trimers. Opportunities also exist for transforming the geometry of the central trimer structure from one that is rounded to one that expresses sharp corners or spiked features using wet chemistry.[68,69] Important to note is that once coated with amorphous Al_2O_3, such features will be preserved at the high temperatures needed to assemble trimers since the oxide coating eliminates the Au surface diffusion pathways that would otherwise see the nanostructures revert to a more rounded shape.[33] It should also prove possible to assert some level of size and shape control over the front and back components of the trimer structures using colloidal chemistry growth modes provided that the amorphous Al_2O_3 layer is able to withstand the chemical environment used. Taken together, there exist significant opportunities for advancing the capabilities beyond those presented here.

CONCLUSION

In summary, a substrate-based assembly process has been demonstrated that gives rise to aligned Au trimers and dimers with air-filled nanogaps. The process forwarded is unique in its use of two sacrificial materials where one sets the nanogap width while the other regulates the high-temperature assembly of Au. The fabrication of dimer and trimer arrays demonstrates the utility of integrating lithographic capabilities into the assembly process as it allows for the periodic placement of plasmonically coupled nanostructures while relaxing the lithographic resolution requirement since it is no longer essential to nanogap definition. Also demonstrated is the effectiveness of using glancing angle depositions and ion milling as additive and subtractive counterparts in nanofabrication schemes designed to induce asymmetries into assembly processes. Taken together, the work presents new avenues for defining photoactive nanomaterials and for the

https://doi.org/10.1021/acsami.2c04800
ACS Appl. Mater. Interfaces 2022, 14, 28186−28198

deterministic placement of plasmonic energy on substrate surfaces.

EXPERIMENTAL SECTION

Chemicals and Materials. Au trimers were assembled on 10.5 mm × 5 mm × 0.6 mm substrates cut from two-side polished wafers of single-crystal [0001]-oriented Al_2O_3 that were sourced from MTI Corp. Au sputter targets with a 19 mm diameter were prepared from 0.5 mm thick Au foil (99.9985% pure, Alfa Aesar) using a punch and die setup. Sb sputter targets with approximately the same dimensions were sliced from a 99.999% pure rod (ESPI Metals). Nanoimprint lithography processes utilized Si stamps purchased from Lightsmyth Technologies, a trichloro(1*H*,2*H*,2*H*-perfluorooctyl)silane antisticking layer (MilliporeSigma), and a 7030R thermal resist (Micro Resist Technology, GmbH). All assembly processes were carried out in ultrahigh purity Ar gas (Airgas). ALD depositions used a trimethylaluminum (TMA) precursor sourced from Millipore Sigma. Amorphous Al_2O_3 etching was carried out using NaOH (Sigma-Aldrich) and deionized (DI) H_2O derived from a Milli-Q system with a resistivity of 18.2 MΩ·cm. TEM work was carried out using silicon nitride TEM window grids (SIMPore Inc.) with a window thickness of 20 nm. SERS analysis utilized benzenethiol (i.e., thiophenol) (≥99%, Sigma-Aldrich). Refractive index sensitivity measurements used acetonitrile (BDH Chemicals) and toluene (Beantown Chemical).

Formation of Oxide-Coated Au Nanostructures. The central component of trimer was formed by sequentially sputter-depositing thin films of Sb (10.5 nm) and Au (3.2 nm) onto a sapphire substrate at room temperature using two Penning ion guns (Ar pressure 7 × 10^{-5} Torr, current 200 μA, voltage 6 keV). The deposition rates for Sb and Au are 0.3 and 0.2 nm·s^{-1}, respectively. The deposited films are then placed in an alumina crucible that is inserted into a quartz tube furnace under an Ar flow of 120 cm^3·min^{-1}. Once residual air is purged from the system (≈ 30 min), the flow is reduced to 60 cm^3·min^{-1}, and the sample is subjected to a heating regimen that sees it heated to 1085 °C in 26 min followed by a 45 min cool-down to room temperature. This process yields standalone Au nanostructures that are well-separated. Structures formed directly on TEM grids were made in an identical manner except that the processing temperature was reduced to 900 °C due to the fragility of Si_3N_4 membrane. Conformal Al_2O_3 layers were applied over the standalone Au nanostructures as well as the exposed substrate using ALD. The deposition proceeds at 200 °C by sequentially exposing the surface to two precursors (i.e., TMA, H_2O) in a pulsed, alternating, and nonoverlapping manner where each pulse results in a self-limiting half-reaction. The exposure times used for TMA, H_2O, and the N_2 purge gas are 20 ms, 20 ms, and 7 s, respectively. The desired thickness is obtained by adjusting the number of deposition cycles as demanded by an ellipsometry-based thickness calibration carried out as part of a prior study.[33] As is typical for ALD-deposited Al_2O_3, the resulting layer is amorphous where the exact stoichiometry is ill-defined.

Trimer Formation. Sb and Au are sequentially deposited onto the oxide-coated Au nanostructures at a glancing angle of 10° and a target-to-substrate distance of approximately 4.7 cm. The thicknesses of the Sb and Au layers if the deposited material were to land on an identically angled blank substrate are 7.8 and 5.5 nm, respectively. Trimers are assembled in a quartz tube furnace under an Ar flow (120 cm^3·min^{-1}) using a heating regimen that sees the sample heated to 550 °C in 7 min and held there for 40 min before a slow cool to room temperature. This process yields trimers with Al_2O_3 nanogaps. Air-filled nanogaps were formed by etching the amorphous Al_2O_3 at room temperature in a 5 mL aqueous solution of 10 mM NaOH. The optimum etching time for all nanogap thicknesses is approximately 25 min (Figure S8).

Periodic Arrays of Au Dimers and Trimers. Hexagonal arrays of standalone Au nanostructures with a diameter of 75 nm and a center-to-center distance of 600 nm were fabricated using NIL in combination with a directed-assembly process, the details of which are described elsewhere.[66,67] A 5 nm conformal layer of amorphous Al_2O_3 was then applied to the surface using the aforementioned ALD deposition parameters. These standalone structures were transformed into dimers by first depositing Sb and Au layers at a glancing angle of 5° with nominal thicknesses of 2.6 and 2.7 nm, respectively. The coated surface is then exposed to an oppositely directed glancing angle ion milling procedure that sees a 0.1 keV collimated Ar^+ ion beam directed at a 9° angle for 10 s. Dimer assembly then occurs using the previously described parameters. Trimer formation proceeds by first forming a dimer array and then exposing it to the same glancing angle deposition and milling procedures but where the in-plane placement of the sample is rotated by 180° when compared to that used for the dimers. All ion milling procedures were carried out over a 3 mm^2 area, a value that is limited by the instrumentation used as opposed to the technique itself. The high-temperature trimer assembly process is identical to that used for dimers.

Optical Characterization. SERS measurements were carried out on trimer samples with air-filled nanogaps with 3−8 nm widths where, in all cases, the Al_2O_3 spacer material was etched using conditions optimized for the 5 nm width. The reporter molecule was applied to the trimers over a 48 h period using gas phase adsorption in which all samples were simultaneously placed in a sealed Petri dish along with a vial containing 40 μL of neat benzenethiol. After the incubation period, the substrates were removed and blown with air. Spectra, with 60 s exposure times, were collected using a home-built setup in which a 633 nm HeNe laser (Thorlabs) is directed into a Nikon Ti-U inverted microscope after which it is focused onto the sample using an objective lens (20×, NA = 0.5). The laser power, as measured at the objective, is 4 mW. The scattered light is collected using the same objective, passed through a Semrock Rayleigh rejection filter, and then directed into a Princeton Instruments Action SP2300 spectrometer (f = 0.3 mm, 1200 g·mm^{-1}). The Zhang algorithm[70] was used to perform the baseline subtraction. Polarization-dependent SERS spectra utilized a 785 nm laser (785C-45-CDRH, Spectra Physics) with a 3 mW power at the objective and 10 s exposure times. Refractive index sensitivity data were collected by placing the Au trimer sample that had been optimally etched into a liquid-filled cuvette in the upright position. Spectra were taken with light polarized parallel and perpendicular to the long axis of the trimer. The liquids used, which consist of a mixture of acetonitrile and toluene with variable molar fractions, allowed for index of refraction variations between 1.346 and 1.496.

Instrumentation. A model 681 Gatan high resolution ion beam coater was used for all sputter depositions. Nanostructure assembly was carried out in a Lindberg Blue M furnace fitted with a quartz tube and an Ar gas handling system. ALD depositions were made using a Cambridge Savannah S100 system. Glancing angle ion milling procedures were carried out in a 685 Gatan PECS II system. SEM images and EDS spectra were obtained using a Helios G4 Ux SEM/FIB workstation (FEI). TEM and NBD were carried out on an FEI Talos F200X field emission microscope operated at 200 kV. Extinction spectra were obtained using a JASCO V-730 UV−visible spectrophotometer fitted with linear polarizers.

ASSOCIATED CONTENT

Supporting Information

The Supporting Information is available free of charge at https://pubs.acs.org/doi/10.1021/acsami.2c04800.

Nanostructure characterization in the form of SEMs, EDS, SERS, and extinction spectra and refractive index sensitivity plots; description of methodology used for simulations; simulations of the extinction and EF spectra for transverse plasmon modes; schematics of the GLAD setup and geometric models used in simulations (PDF)

Video S1 showing the near-fields for the 610 nm resonance by scanning through cross sections parallel to the substrate beginning near the top of the structure and moving downward (AVI)

https://doi.org/10.1021/acsami.2c04800
ACS Appl. Mater. Interfaces 2022, 14, 28186−28198

Video S2 showing the near-fields for the 610 nm resonance by scanning through cross sections perpendicular to the substrate beginning near the outer edge of the structure and moving to its midsection (AVI)

Video S3 showing the near-fields for the 687 nm resonance by scanning through cross sections parallel to the substrate beginning near the top of the structure and moving downward (AVI)

Video S4 showing the near-fields for the 687 nm resonance by scanning through cross sections perpendicular to the substrate beginning near the outer edge of the structure and moving to its midsection (AVI)

AUTHOR INFORMATION

Corresponding Authors

Jost Adam − *Computational Materials Group, SDU Centre for Photonics Engineering, Mads Clausen Institute, University of Southern Denmark, 5230 Odense, Denmark*; Email: jostadam@sdu.dk

Svetlana Neretina − *College of Engineering and Department of Chemistry and Biochemistry, University of Notre Dame, Notre Dame, Indiana 46556, United States*; orcid.org/0000-0002-6889-4384; Email: sneretina@nd.edu

Authors

Zachary R. Lawson − *College of Engineering, University of Notre Dame, Notre Dame, Indiana 46556, United States*

Arin S. Preston − *College of Engineering, University of Notre Dame, Notre Dame, Indiana 46556, United States*

Matiyas T. Korsa − *Computational Materials Group, SDU Centre for Photonics Engineering, Mads Clausen Institute, University of Southern Denmark, 5230 Odense, Denmark*

Nathaniel L. Dominique − *Department of Chemistry and Biochemistry, University of Notre Dame, Notre Dame, Indiana 46556, United States*; orcid.org/0000-0002-0439-9982

Walker J. Tuff − *College of Engineering, University of Notre Dame, Notre Dame, Indiana 46556, United States*

Eli Sutter − *Department of Mechanical and Materials Engineering, University of Nebraska-Lincoln, Lincoln, Nebraska 68588, United States*; orcid.org/0000-0002-6939-2714

Jon P. Camden − *Department of Chemistry and Biochemistry, University of Notre Dame, Notre Dame, Indiana 46556, United States*; orcid.org/0000-0002-6179-2692

Robert A. Hughes − *College of Engineering, University of Notre Dame, Notre Dame, Indiana 46556, United States*

Complete contact information is available at: https://pubs.acs.org/10.1021/acsami.2c04800

Author Contributions

⊥Z.R.L., A.S.P., and M.T.K. contributed equally.

Notes

The authors declare no competing financial interest.

ACKNOWLEDGMENTS

This work was supported by the National Science Foundation, Civil, Mechanical and Manufacturing Innovation, Advanced Manufacturing Program under Grant CMMI-1911991 as well as a Notre Dame NDnano Seed Grant Award to S.N. The computational calculations (J.A.) were conducted with support of the UCloud services provided by the eScience Center at SDU. The TEM investigation (E.S.) was supported by the National Science Foundation, Division of Materials Research, Solid State and Materials Chemistry Program under Grant DMR-1904843. The SERS investigation (J.P.C.) was supported by the National Science Foundation, Division of Chemistry, Macromolecular, Supramolecular, and Nanochemistry Program under Grant CHE-2108330. W.J.T. acknowledges support received through a Notre Dame Materials Science and Engineering Fellowship. The work has benefited from the facilities available through the Notre Dame Integrated Imaging Facility (NDIIF).

REFERENCES

(1) Ding, S.-Y.; Yi, J.; Li, J.-F.; Ren, B.; Wu, D.-Y.; Panneerselvam, R.; Tian, Z.-Q. Nanostructure-Based Plasmon-Enhanced Raman Spectroscopy for Surface Analysis of Materials. *Nat. Rev. Mater.* **2016**, *1*, 16021.

(2) Luk'yanchuk, B.; Zheludev, N. I.; Maier, S. A.; Halas, N. J.; Nordlander, P.; Giessen, H.; Chong, C. T. The Fano Resonance in Plasmonic Nanostructures and Metamaterials. *Nat. Mater.* **2010**, *9*, 707−715.

(3) Bigelow, N. W.; Vaschillo, A.; Camden, J. P.; Masiello, D. J. Signatures of Fano Interferences in the Electron Energy Loss Spectroscopy and Cathodoluminescence of Symmetry-Broken Nanorod Dimers. *ACS Nano* **2013**, *7*, 4511−4519.

(4) Manuel, A. P.; Kirkey, A.; Mahdi, N.; Shankar, K. Plexcitonics - Fundamental Principles and Optoelectronic Applications. *J. Mater. Chem. C* **2019**, *7*, 1821−1853.

(5) Schlather, A. E.; Large, N.; Urban, A. S.; Nordlander, P.; Halas, N. J. Near-Field Mediated Plexcitonic Coupling and Giant Rabi Splitting in Individual Metallic Dimers. *Nano Lett.* **2013**, *13*, 3281−3286.

(6) Hartland, G. V.; Besteiro, L. V.; Johns, P.; Govorov, A. O. What's So Hot about Electrons in Metal Nanoparticles? *ACS Energy Lett.* **2017**, *2*, 1641−1653.

(7) Lee, J.; Jeon, D. J.; Yeo, J. S. Quantum Plasmonics: Energy Transport through Plasmonic Gap. *Adv. Mater.* **2021**, *33*, 2006606.

(8) Smolsky, J.; Kaur, S.; Hayashi, C.; Batra, S. K.; Krasnoslobodtsev, A. V. Surface-Enhanced Raman Scattering-Based Immunoassay Technologies for Detection of Disease Biomarkers. *Biosensors* **2017**, *7*, 7.

(9) Huang, Z.; Zhang, A.; Zhang, Q.; Cui, D. Nanomaterial-Based SERS Sensing Technology for Biomedical Application. *J. Mater. Chem. B* **2019**, *7*, 3755−3774.

(10) Hakonen, A.; Andersson, P. O.; Schmidt, M. S.; Rindzevicius, T.; Käll, M. Explosive and Chemical Threat Detection by Surface-Enhanced Raman Scattering: A Review. *Anal. Chim. Acta* **2015**, *893*, 1−13.

(11) Bodelón, G.; Pastoriza-Santos, I. Recent Progress in Surface-Enhanced Raman Scattering for the Detection of Chemical Contaminants in Water. *Front. Chem.* **2020**, *8*, 478.

(12) de Oliveira Penido, C. A. F.; Pacheco, M. T. T.; Lednev, I. K.; Silveira, L., Jr. Raman Spectroscopy in Forensic Analysis: Identification of Cocaine and Other Illegal Drugs of Abuse. *J. Raman Spectrosc.* **2016**, *47*, 28−38.

(13) Kumar, A.; Choudhary, P.; Kumar, A.; Camargo, P. H. C.; Krishnan, V. Recent Advances in Plasmonic Photocatalysis Based on TiO_2 and Noble Metal Nanoparticles for Energy Conversion, Environmental Remediation, and Organic Synthesis. *Small* **2022**, *18*, 2101638.

(14) Gellé, A.; Moores, A. Plasmonic Nanoparticles: Photocatalysts with a Bright Future. *Curr. Opin. Green Sust.* **2019**, *15*, 60−66.

(15) Li, J.-F.; Li, C.-Y.; Aroca, R. F. Plasmon-Enhanced Fluorescence Spectroscopy. *Chem. Soc. Rev.* **2017**, *46*, 3962−3979.

(16) Qiao, F.; Xie, Y.; He, G.; Chu, H.; Liu, W.; Chen, Z. Light Trapping Structures and Plasmons Synergistically Enhance the Photovoltaic Performance of Full-Spectrum Solar Cells. *Nanoscale* **2020**, *12*, 1269.

(17) Kim, J. M.; Lee, C.; Lee, Y.; Lee, J.; Park, S.-J.; Park, S.; Nam, J.-M. Synthesis, Assembly, Optical Properties, and Sensing Applications of Plasmonic Gap Nanostructures. *Adv. Mater.* **2021**, *33*, 2006966.
(18) Yang, Y.; Gu, C.; Li, J. Sub-5 nm Metal Nanogaps: Physical Properties, Fabrication Methods, and Device Applications. *Small* **2019**, *15*, 1804177.
(19) Gu, P.; Zhang, W.; Zhang, G. Plasmonic Nanogaps: From Fabrications to Optical Applications. *Adv. Mater. Interfaces* **2018**, *5*, 1800648.
(20) Jain, T.; Westerlund, F.; Johnson, E.; Moth-Poulsen, K.; Bjørnholm, T. Self-Assembled Nanogaps *via* Seed-Mediated Growth of End-to-End Linked Gold Nanorods. *ACS Nano* **2009**, *3*, 828−834.
(21) Gilroy, K. D.; Xia, Y. Dimerization of Colloidal Particles through Controlled Aggregation for Enhanced Properties and Applications. *Chem.—Asian J.* **2016**, *11*, 2341−2351.
(22) Yoon, J. H.; Selbach, F.; Langolf, L.; Schlücker, S. Ideal Dimers of Gold Nanospheres for Precision Plasmonics: Synthesis and Characterization at the Single-Particle Level for Identification of Higher Order Modes. *Small* **2018**, *14*, 1702754.
(23) Kim, M.; Kwon, H.; Lee, S.; Yoon, S. Effect of Nanogap Morphology on Plasmon Coupling. *ACS Nano* **2019**, *13*, 12100−12108.
(24) Lai, Y.; Cui, X.; Li, N.; Shao, L.; Zhang, W.; Wang, J.; Lin, H. Q. Asymmetric Light Scattering on Heterodimers Made of Au Nanorods Vertically Standing on Au Nanodisks. *Adv. Optical Mater.* **2021**, *9*, 2001595.
(25) Zhou, W.; Liu, Z.; Huang, Z.; Lin, H.; Samanta, D.; Lin, Q.-Y.; Aydin, K.; Mirkin, C. A. Device-Quality, Reconfigurable Metamaterials from Shape-Directed Nanocrystal Assembly. *Proc. Natl. Acad. Sci. U. S. A.* **2020**, *117*, 21052−21057.
(26) Yang, F.; Ye, S.; Dong, W.; Zheng, Di; Xia, Y.; Yi, C.; Tao, J.; Sun, C.; Zhang, L.; Wang, L.; Chen, Q.; Wang, Y.; Nie, Z. Laser-Scanning-Guided Assembly of Quasi-3D Patterned Arrays of Plasmonic Dimers for Information Encryption. *Adv. Mater.* **2021**, *33*, 2100325.
(27) Ni, S.; Isa, L.; Wolf, H. Capillary Assembly as a Tool for the Heterogeneous Integration of Micro- and Nanoscale Objects. *Soft Matter* **2018**, *14*, 2978−2995.
(28) Masango, S. S.; Hackler, R. A.; Large, N.; Henry, A.-I.; McAnally, M. O.; Schatz, G. C.; Stair, P. C.; Van Duyne, R. P. High-Resolution Distance Dependence Study of Surface-Enhanced Raman Scattering Enabled by Atomic Layer Deposition. *Nano Lett.* **2016**, *16*, 4251−4259.
(29) Johnson, R. W.; Hultqvist, A.; Bent, S. F. A Brief Review of Atomic Layer Deposition: From Fundamentals to Applications. *Mater. Today* **2014**, *17*, 236−246.
(30) Im, H.; Bantz, K. C.; Lee, S. H.; Johnson, T. W.; Haynes, C. L.; Oh, S. H. Self-Assembled Plasmonic Nanoring Cavity Arrays for SERS and LSPR Biosensing. *Adv. Mater.* **2013**, *25*, 2678−2685.
(31) Hu, Z.; Liu, Z.; Li, L.; Quan, B.; Li, Y.; Li, J.; Gu, C. Wafer-Scale Double-Layer Stacked Au/Al_2O_3 @Au Nanosphere Structure with Tunable Nanospacing for Surface-Enhanced Raman Scattering. *Small* **2014**, *10*, 3933−3942.
(32) Jeong, H.-H.; Adams, M. C.; Günther, J.-P.; Alarcón-Correa, M.; Kim, I.; Choi, E.; Miksch, C.; Mark, A. F.; Mark, A. G.; Fischer, P. Arrays of Plasmonic Nanoparticle Dimers with Defined Nanogap Spacers. *ACS Nano* **2019**, *13*, 11453−11459.
(33) Preston, A. S.; Hughes, R. A.; Demille, T. B.; Neretina, S. Plasmonics under Attack: Protecting Copper Nanostructures from Harsh Environments. *Chem. Mater.* **2020**, *32*, 6788−6799.
(34) Preston, A. S.; Hughes, R. A.; Dominique, N. L.; Camden, J. P.; Neretina, S. Protecting Plasmonic Silver Nanostructures with Ultrathin Oxide Coatings Deposited using Atomic Layer Deposition. *J. Phys. Chem. C* **2021**, *125*, 17212−17220.
(35) Albrecht, G.; Kaiser, S.; Giessen, H.; Hentschel, M. Refractory Plasmonics without Refractory Materials. *Nano Lett.* **2017**, *17*, 6402−6408.
(36) Albrecht, G.; Ubl, M.; Kaiser, S.; Giessen, H.; Hentschel, M. Comprehensive Study of Plasmonic Materials in the Visible and Near-Infrared: Linear, Refractory, and Nonlinear Optical Properties. *ACS Photonics* **2018**, *5*, 1058−1067.
(37) Prakash, J.; Swart, H. C.; Zhang, G.; Sun, S. Emerging Applications of Atomic Layer Deposition for the Rational Design of Novel Nanostructures for Surface-Enhanced Raman Scattering. *J. Mater. Chem. C* **2019**, *7*, 1447−1471.
(38) Namgung, S.; Koester, S. J.; Oh, S.-H. Ultraflat Sub-10 Nanometer Gap Electrodes for Two-Dimensional Optoelectronic Devices. *ACS Nano* **2021**, *15*, 5276−5283.
(39) Chen, X.; Park, H. R.; Pelton, M.; Piao, X.; Lindquist, N. C.; Im, H.; Kim, Y. J.; Ahn, J. S.; Ahn, K. J.; Park, N.; Kim, D. S.; Oh, S. H. Atomic Layer Lithography of Wafer-Scale Nanogap Arrays for Extreme Confinement of Electromagnetic Waves. *Nat. Commun.* **2013**, *4*, 2361.
(40) Park, H. R.; Chen, X.; Nguyen, N.-C.; Peraire, J.; Oh, S.-H. Nanogap-Enhanced Terahertz Sensing of 1 nm Thick ($\lambda/10^6$) Dielectric Films. *ACS Photonics* **2015**, *2*, 417−424.
(41) Chen, X.; Ciracì, C.; Smith, D. R.; Oh, S. H. Oh Nanogap-Enhanced Infrared Spectroscopy with Template-Stripped Wafer-Scale Arrays of Buried Plasmonic Cavities. *Nano Lett.* **2015**, *15*, 107−113.
(42) Yoo, D.; Nguyen, N.-C.; Martin-Moreno, L.; Mohr, D. A.; Carretero-Palacios, S.; Shaver, J.; Peraire, J.; Ebbesen, T. W.; Oh, S. H. High-Throughput Fabrication of Resonant Metamaterials with Ultrasmall Coaxial Apertures via Atomic Layer Lithography. *Nano Lett.* **2016**, *16*, 2040−2046.
(43) Ji, D.; Cheney, A.; Zhang, N.; Song, H.; Gao, J.; Zeng, X.; Hu, H.; Jiang, S.; Yu, Z.; Gan, Q. Efficient Mid-Infrared Light Confinement within Sub-5-nm Gaps for Extreme Field Enhancement. *Adv. Optical Mater.* **2017**, *5*, 1700223.
(44) Li, C.; Jin, Y. Shell-Isolated Plasmonic Nanostructures for Biosensing, Catalysis, and Advanced Nanoelectronics. *Adv. Funct. Mater.* **2021**, *31*, 2008031.
(45) Baumberg, J. J.; Aizpurua, J.; Mikkelsen, M. H.; Smith, D. R. Extreme Nanophotonics from Ultrathin Metallic Gaps. *Nat. Mater.* **2019**, *18*, 668−678.
(46) Im, H.; Bantz, K. C.; Lindquist, N. C.; Haynes, C. L.; Oh, S.-H. Vertically Oriented Sub-10-nm Plasmonic Nanogap Arrays. *Nano Lett.* **2010**, *10*, 2231−2236.
(47) Cao, Y. Q.; Qin, K.; Zhu, L.; Qian, X.; Zhang, X. J.; Wu, D.; Li, A. D. Atomic-Layer-Deposition Assisted Formation of Wafer-Scale Double-Layer Metal Nanoparticles with Tunable Nanogap for Surface-Enhanced Raman Scattering. *Sci. Rep.* **2017**, *7*, 5161.
(48) Hawkeye, M. M.; Brett, M. J. Glancing Angle Deposition: Fabrication, Properties, and Applications of Micro- and Nanostructured Thin Films. *J. Vac. Sci. Technol. A* **2007**, *25*, 1317−1335.
(49) Mark, A. G.; Gibbs, J. G.; Lee, T.-C.; Fischer, P. Hybrid Nanocolloids with Programmed Three-Dimensional Shape and Material Composition. *Nat. Mater.* **2013**, *12*, 802−807.
(50) Ai, B.; Zhao, Y. Glancing Angle Deposition Meets Colloidal Lithography: A New Evolution in the Design of Nanostructures. *Nanophotonics* **2018**, *8*, 1−26.
(51) Zhang, M.; Large, N.; Koh, A. L.; Cao, Y.; Manjavacas, A.; Sinclair, R.; Nordlander, P.; Wang, S. X. High-Density 2D Homo- and Hetero-Plasmonic Dimers with Universal Sub-10-nm Gaps. *ACS Nano* **2015**, *9*, 9331−9339.
(52) Lin, Y.; Wang, D.; Hu, J.; Liu, J.; Wang, W.; Guan, J.; Schaller, R. D.; Odom, T. W. Engineering Symmetry-Breaking Nanocrescent Arrays for Nanolasing. *Adv. Funct. Mater.* **2019**, *29*, 1904157.
(53) Farzinpour, P.; Sundar, A.; Gilroy, K. D.; Eskin, Z. E.; Hughes, R. A.; Neretina, S. Altering the Dewetting Characteristics of Ultrathin Gold and Silver Films using a Sacrificial Antimony Layer. *Nanotechnology* **2012**, *23*, 495604.
(54) Farzinpour, P.; Sundar, A.; Gilroy, K. D.; Eskin, Z. E.; Hughes, R. A.; Neretina, S. Dynamic Templating: A Large Area Processing Route for the Assembly of Periodic Arrays of Sub-Micrometer and Nanoscale Structures. *Nanoscale* **2013**, *5*, 1929−1938.
(55) Thompson, C. V. Solid-State Dewetting of Thin Films. *Annu. Rev. Mater. Res.* **2012**, *42*, 399−434.

https://doi.org/10.1021/acsami.2c04800
ACS Appl. Mater. Interfaces 2022, 14, 28186−28198

(56) Golze, S. D.; Hughes, R. A.; Menumerov, E.; Rouvimov, S.; Neretina, S. Synergistic Roles of Vapor- and Liquid-Phase Epitaxy in the Seed-Mediated Synthesis of Substrate-Based Noble Metal Nanostructures. *Nanoscale* **2021**, *13*, 20225−20233.
(57) Vazquez-Mena, O.; Sannomiya, T.; Villanueva, L. G.; Voros, J.; Brugger, J. Metallic Nanodot Arrays by Stencil Lithography for Plasmonic Biosensing Applications. *ACS Nano* **2011**, *5*, 844−853.
(58) Broas, M.; Kanninen, O.; Vuorinen, V.; Tilli, M.; Paulasto-Kröckel, M. Chemically Stable Atomic-Layer-Deposited Al_2O_3 Films for Processability. *ACS Omega* **2017**, *2*, 3390−3398.
(59) Verellen, N.; Sonnefraud, Y.; Sobhani, H.; Hao, F.; Moshchalkov, V. V.; Van Dorpe, P.; Nordlander, P.; Maier, S. A. Fano Resonances in Individual Coherent Plasmonic Nanocavities. *Nano Lett.* **2009**, *9*, 1663−1667.
(60) Whelan, C. M.; Smyth, M. R.; Barnes, C. J. HREELS, XPS, and Electrochemical Study of Benzenethiol Adsorption on Au(111). *Langmuir* **1999**, *15*, 116−126.
(61) Marhaba, S.; Bachelier, G.; Bonnet, C.; Broyer, M.; Cottancin, E.; Grillet, N.; Lermé, J.; Vialle, J. L.; Pellarin, M. Surface Plasmon Resonance of Single Gold Nanodimers near the Conductive Contact Limit. *J. Phys. Chem. C* **2009**, *113*, 4349−4356.
(62) Cha, H.; Yoon, J. H.; Yoon, S. Probing Quantum Plasmon Coupling Using Gold Nanoparticle Dimers with Tunable Interparticle Distances Down to the Subnanometer Range. *ACS Nano* **2014**, *8*, 8554−8563.
(63) Zhang, W.; Li, Q.; Qiu, M. A Plasmon Ruler Based on Nanoscale Photothermal Effect. *Opt. Express* **2013**, *21*, 172−181.
(64) Hughes, R. A.; Menumerov, E.; Neretina, S. When Lithography Meets Self-Assembly: A Review of Recent Advances in the Directed Assembly of Complex Metal Nanostructures on Planar and Textured Surfaces. *Nanotechnology* **2017**, *28*, 282002.
(65) Barad, H.; Kwon, H.; Alarcon-Correa, M.; Fischer, P. Large Area Patterning of Nanoparticles and Nanostructures: Current Status and Future Prospects. *ACS Nano* **2021**, *15*, 5861−5875.
(66) Golze, S. D.; Hughes, R. A.; Rouvimov, S.; Neal, R. D.; Demille, T. B.; Neretina, S. Plasmon-Mediated Synthesis of Periodic Arrays of Gold Nanoplates using Substrate-Immobilized Seeds Lined with Planar Defects. *Nano Lett.* **2019**, *19*, 5653−5660.
(67) Menumerov, E.; Golze, S. D.; Hughes, R. A.; Neretina, S. Arrays of Highly Complex Noble Metal Nanostructures using Nanoimprint Lithography in Combination with Liquid-Phase Epitaxy. *Nanoscale* **2018**, *10*, 18186−18194.
(68) Preston, A. S.; Hughes, R. A.; Demille, T. B.; Rey Davila, V. M.; Neretina, S. Dewetted Nanostructures of Gold, Silver, Copper, and Palladium with Enhanced Faceting. *Acta Mater.* **2019**, *165*, 15−25.
(69) Demille, T. B.; Hughes, R. A.; Dominique, N.; Olson, J. E.; Rouvimov, S.; Camden, J. P.; Neretina, S. Large-Area Periodic Arrays of Gold Nanostars Derived from HEPES-, DMF-, and Ascorbic-Acid-Driven Syntheses. *Nanoscale* **2020**, *12*, 16489−16500.
(70) Zhang, Z. M.; Chen, S.; Liang, Y. Z. Baseline Correction using Adaptive Iteratively Reweighted Penalized Least Squares. *Analyst* **2010**, *135*, 1138−1146.

https://doi.org/10.1021/acsami.2c04800
ACS Appl. Mater. Interfaces 2022, 14, 28186−28198